EAI Endorsed Transactions
on Internet of Things
Research Article EAI.EU

Glaucoma Retinal Image Detection through the Segmentation of OD Using Modified Deep Learning Method

J.Ruby Elizabeth[1,*], D.Kesavaraja[2], S.Ebenezer Juliet[3], S.Jagadeesh[4], S.Samsudeen Shaffi[4], R.Umanesan[4]

[1]Computer Science and Business Systems, Nehru Institute of Engineering and Technology, Coimbatore, Tamilnadu, India
[2]Department of Computer Science and Engineering, Dr. Sivanthi Aditanar College of Engineering, Tuticorin, Tamilnadu, India
[3]SCOPE, VIT, Vellore, Tamilnadu, India
[4,5,6]Department of Computer Science and Engineering, Vel Tech Rangarajan Dr. Sagunthala R&D Institute of Science and Technology, Chennai, Tamilnadu, India

Abstract

Classifiers are the important processing module in any type of classification systems. This paper uses the proposed Modified LeNET (MLNET) classification architecture along with the standard LeNET to classify the retinal pictures into healthy cases and cases of glaucoma. This research work develops an automated computer aided system which has the following modules as preprocessing, Optic Disk (OD) segmentation, Feature computations and MLNET classification. The Glaucoma classification system has been functioned in two processing phases as training and testing. The training processing phase trains both healthy and Glaucoma retinal images from the known dataset using preprocessing, OD segmentation and feature computations from the segmented OD region. These features from the OD region have been further trained by the proposed MLNET classifier. The testing processing phase tests the unknown retinal image into either Glaucoma or healthy class through the sub processing modules of preprocessing, OD region segmentation and feature computations. The features from the OD region in the unknown test retinal image have been fed into the proposed MLNET classifier with respect to the previous training results.

Keywords: Classifiers, Glaucoma, dataset, retinal image, features

Received on 24 August 2025, accepted on 10 November 2025, published on 26 November 2025

doi: 10.4108/eetiot.10062

*Corresponding author. Email: nietjrubyelizabeth@nehrucolleges.com

1. Introduction

The chronic condition glaucoma is known as the silent thief of sight since it never shows any signs. If glaucoma is not detected in its early stages, it can cause irreversible blindness. Peripheral vision loss is caused by an improvement in the Cup to Disc Ratio (CDR) following glaucoma. Visual impairment is used to define glaucoma disease based on optic disc cupping and optic nerve fibre degeneration [1-5]. The progressive optic neuropathy known as glaucoma causes damage to the retinal ganglion cells and axons resulting in changes in the visual field. The disease known as glaucoma is brought on by the neurodegeneration of the optic nerve, which ultimately causes blindness. Monitoring Intra Ocular Pressure (IOP), the visual field, and the appearance of the optic disc (Cup-to-Disc Ratio) are used to assess it. It is evident from completing the poll that one million Indians over 40 suffer from glaucoma.

Ophthalmologists can detect glaucoma early and halt its progression thanks to structural changes in the retina that occur as the disease progresses. The relationship between light receptors and the visual brain becomes less significant as the disease progresses. It changed the size of the cup and reduced the retina's functioning abilities. CDR is used to track the development of glaucoma [6-9].

According to the World Health Organisation, glaucoma accounts for 15% of blindness and is the second most common cause of blindness. The fluid produced by the eye causes an increase in intraocular pressure, which is the first sign of glaucoma. The equilibrium is maintained in a normal eye because the amount of liquid generated and the amount of liquid released by the eye are equal. Liquid does not drain from the eye in glaucoma, which increases ocular stress and damages the optic nerve, which is in charge of brain-to-eye communication. Over time, the increase in pressure causes the optic nerve to be destroyed, resulting in permanent blindness.

2. Literature Survey

Nasrollahi et al. [10] used the eye's IOP to track the development of glaucoma. The use of medicine to lower IOP can help to slow down the course of glaucoma. Nevertheless, a solitary IOP measurement taken during a clinical visit never yields information regarding circadian rhythm. Thus, the IOP is measured several times a day by examining the interaction between single waves and the eye. The striker, an electromagnetic device trigger circuit, a wave measuring sensor, and an electronic reader circuit to process reflected signals produce the solitary waves. Once the waves came into contact with the eye, they took on unique characteristics. The unique characteristics' numerical analysis revealed a monotonic association with the eye's IOP. Gifta Jerith et al. [11] created the Grey Wolf Optimised Neural Network (GWO-NN), a glaucoma detection technique, to determine whether a patient has the condition or not. The input image was transformed to grayscale during the preprocessing stage in order to remove noise using the Adaptive Median Filter (AMF). Grey Level Co-occurrence Matrix features, Accelerated Robust Feature, and Histogram of Oriented Gradients features from the processed image were used to extract the features.

By utilising phylogenetic diversity indices in retinal pictures, Marcos Vinícius dos Santos Ferreira et al. [12] presented a deep learning strategy for automatic glaucoma detection that explores texture properties. Convolutional neural networks were trained to acquire images from databases in order to segment optical discs. It was imperative that blood vessel removal be carried out following the feature extraction procedure from RGB channels and grey levels. The retrieved qualities were dependent on the phylogenetic diversity indexes-derived textural features. Mohammed El Amine Bechar et al. [13] presented Super Pixels for Semi-Supervised Segmentation (SP3S), an automated glaucoma screening method consisting of three phases. Using the superpixel approach to label the superpixels, labelled and unlabeled data were arranged in the first phase. Colour and spatial information were used to introduce the concepts of optic cups and discs. In order to build a robust classifier, a semi-supervised learning Co-forest classifier was trained using a large number of labelled and unlabelled superpixels. Yujie et al. [14] used input photos to conduct transfer learning of Convolutional Neural Networks (CNNs). A grayscale picture of the optic disc's fundus was used. The CNN was trained using dropout and data augmentation. Random Forest (RF) was used to combine the outputs from each CNN model and classify the disc fundus photos of both healthy and glaucomatous eyes. Each input image's feature vector representation was created by eliminating the second fully connected layer. Pavithra et al. [15] used a revamped artificial neural network with back propagation algorithm concepts to perform the main glaucoma detection. The processing of the cup and disc was done using the morphological operator concepts. The characteristics of the captured disc and cup were discovered using CDR detection concepts through a redesigned feature extraction approach. Whether the input test image was glucomatic or not is declared by the final results. However, primary glaucoma detection did not increase the sensitivity level. Hanan Alghmdi et al. [16] presented an automated method for calculating the Cup to Disc Ratio (CDR) in glaucoma screening. Superpixels Linear Iterative Clustering (SLIC) and a feed-forward neural network classifier were used in the planned method. A superpixel feature was taken out and used as a training classifier input. The superpixels in the region of interest were classified using the classifier in order to identify the borders of the optic disc and cup.

3. Proposed Methodologies for Glaucoma Detection Using Deep Learning Techniques

This research work develops an automated computer aided system which has the following modules as pre-processing, OD segmentation, Feature computations and MLNET classification. The Glaucoma classification system has been functioned in two processing phases as training and testing. The training processing phase trains both healthy and Glaucoma retinal images from the known dataset using pre-processing, OD segmentation and feature computations from the segmented OD region. These features from the OD region have been further trained by the proposed MLNET classifier. The testing processing phase test the unknown retinal image into either Glaucoma or healthy class through the sub processing modules of pre-processing, OD region segmentation and feature computations. The features from the OD region in the unknown test retinal image have been fed into the proposed MLNET classifier with respect to the previous training results.

Figure 1 (a) is the Glaucoma image classification using MLNET in training category and Figure 1(b) is the Glaucoma image classification using MLNET in testing category.

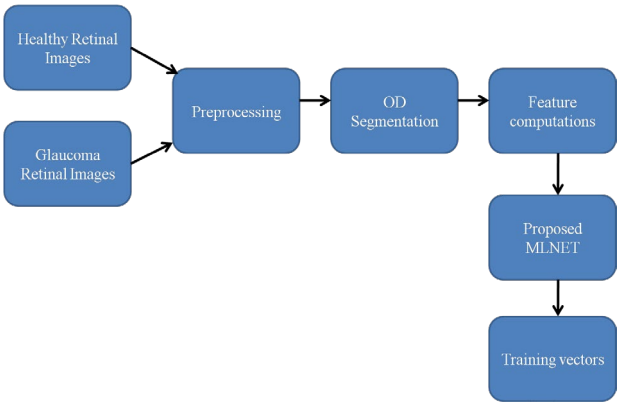

Figure 1(a). Glaucoma image classification using MLNET in training category

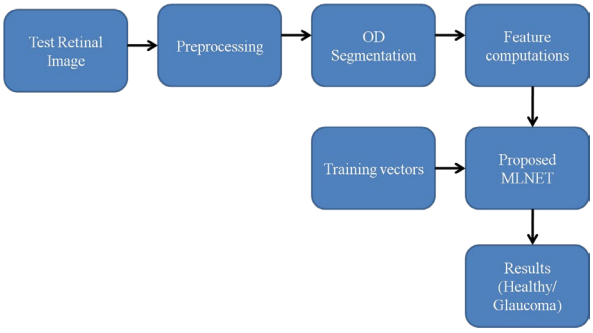

Figure. 1(b). Glaucoma image classification using MLNET in testing category

3.1 Preprocessing

The Glaucoma detection process is depending on the OD region in retinal image and the features computed from the segmented OD region. The preprocessing module is used in this paper to separate the Red component image region from the RGB retinal image. Hence, the red component region has been separated from the source RGB retinal image and the other two component regions have not been further processed.

3.2 OD region segmentation

The retinal blood arteries that supply blood to the entire retina originate in the OD area. In order to obtain the salient characteristics that help distinguish the retinal image of glaucoma from the healthy retinal image, the size of the OD is crucial. Finding and segmenting the OD region in the retinal picture is therefore crucial.
The OD region segmentation process has been illustrated in the following steps.

Algorithm: OD segmentation

Input: separated red component image;
Output: OD segmented region;

Step 1:

The Anisotropic diffusion filter has been applied on source retinal image in order to smooth the region. Figure 2 (a) is the source retinal image and Figure 2 (b) is the Anisotropic diffusion filter output image.

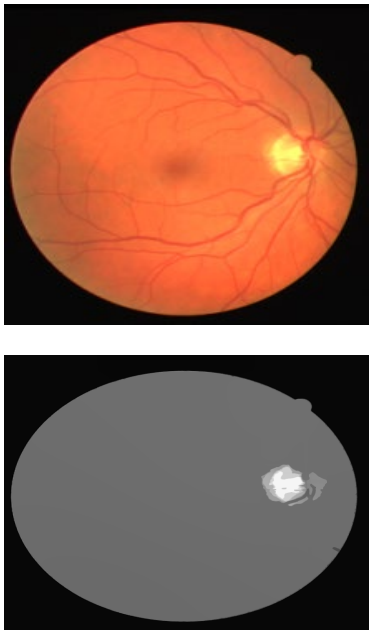

Figure 2 (a). Source retinal image (b) Anisotropic diffusion filter output image

Step 2:

The OD region is belonging to high intensity pixel region in the retinal image. Hence, Apply Connected Component Analysis (CCA) algorithm on the diffusion filtered retinal image to select the high intensity pixel regions in the image, as illustrated in the following equation.

$$c = CCA(diffused\ retinal\ image)$$

Step 3:

Apply morphological filter with 5mm structural pattern on the CCA applied image, as illustrated in the following equation.

$$m = morphological\ (c, 5mm)$$

Step 4:

Subtract the morphological filtered image from the CCA processed retinal image to segment the OD region as illustrated in the following equation.

$$OD\ region = |c - m|$$

Figure 3 is the OD region segmented by the proposed algorithm.

Figure 3. OD region segmented image

3.3 Feature computations

For the purpose of distinguishing the retinal image of glaucoma from the healthy retinal image, the size and form of the segmented OD region are crucial. In order to distinguish the retinal picture of glaucoma from the retinal image of health, the following attributes have been calculated from the segmented OD region and supplied into the suggested MLNET classifier.

$$Computational\ Area\ (CA) = \pi * r^2$$

$$Computational\ Circumference\ (CC) = 2\pi * r$$

$$Computational\ Diameter\ (CD) = 2 * r$$

$$OD\ Heuristic\ Features\ (OHF) = \frac{\sum_{i=1}^{M}\sum_{j=1}^{N} O^2(i,j)}{CA}$$

Whereas, $O(i,j)$ is the segmented OD region with respect to two dimensional vectors i and j.

$$OD\ Linear\ Features\ (OLF) = \frac{\sum_{i=1}^{M}\sum_{j=1}^{N} O^2(i,j)}{CC}$$

$$OD\ Diametric\ Features\ (ODF) = \frac{\sum_{i=1}^{M}\sum_{j=1}^{N} O^2(i,j)}{CD}$$

3.4 Proposed MLNET

The deep learning algorithms play an important role for the classification of features in order to identify the Glaucoma and healthy case retinal images. Most of the researchers for Glaucoma detection process used LeNET algorithm for its simplified and systematic architecture.

The conventional LeNET has been designed with two Convolutional layers (Convolution1, Convolution2) and four pooling layers (pooling1, pooling2) with three FCNN, as illustrated in Figure 4 (a).

The detailed specifications of the Convolutional layers are illustrated in the following equations.

$$Convolutional\ layers = \{Convolution1, Convolution2, Convolution3\}$$

$$Convolution1 = \{32\ kernels, 3 * 3\ kernel\ size\}$$

$$Convolution2 = \{64\ kernels, 5 * 5\ kernel\ size\}$$

The detailed specifications of the Pooling layers are illustrated in the following Equations.

$$Pooling\ layers = \{pooling1, pooling2\}$$

All pooling layers in this conventional LeNET have 3*3 pooling window size with Maximum pooling function.

The detailed specifications of the FCNN layers which are used in the conventional LeNET are illustrated in the following Equations.

$$FCNN = \{FCNN1, FCNN2, FCNN3\}$$

$$FCNN1 = set\ to\ 4096\ neurons$$

$$FCNN2 = set\ to\ 4096\ neurons$$

$$FCNN3 = set\ to\ 2048\ neurons$$

The FCNN3 layer output produces the retinal image classification results as either Glaucoma or healthy case.

Though this LeNET algorithm is simplified for Glaucoma detection process, its detection rate is not optimum in the case of low-resolution retinal images. In order to mitigate this limitation, this conventional LeNET has been modified into proposed MLNET for the Glaucoma retinal image detection process. This MLNET receives the systematic retinal features from the segmented OD region and these features are fed into the MLNET for the Glaucoma detection process. This MLNET has been designed with three Convolutional layers (Convolution1, Convolution2, Convolution3) and four pooling layers (pooling1, polling2, pooling3, pooling4) with three FCNN, as illustrated in Figure 4 (b).

The detailed specifications of the Convolutional layers are illustrated in the following equations.

$$Convolutional\ layers = \{Convolution1, Convolution2, Convolution3\}$$

$$Convolution1 = \{64\ kernels, 3 * 3\ kernel\ size\}$$

$$Convolution2 = \{128\ kernels, 5 * 5\ kernel\ size\}$$

$$Convolution3 = \{256\ kernels, 7 * 7\ kernel\ size\}$$

The detailed specifications of the Pooling layers are illustrated in the following equations.

$$Pooling\ layers = \{pooling1, pooling2, pooling3, pooling4\}$$

All pooling layers in this proposed MLNET have 3*3 pooling window size with Maximum pooling function.

The detailed specifications of the FCNN layers are illustrated in the following equations.

$$FCNN = \{FCNN1, FCNN2, FCNN3\}$$

$$FCNN1 = set\ to\ 4096\ neurons$$

$$FCNN2 = set\ to\ 2048\ neurons$$

$$FCNN3 = set\ to\ 2\ neurons$$

The FCNN3 layer output has been summed up which produces the retinal image classification results.

Figure 4 (a) is the existing LeNET for feature classifications into either Glaucoma or healthy image and Figure 4(b) is the proposed MLNET for feature classifications into either Glaucoma or healthy image.

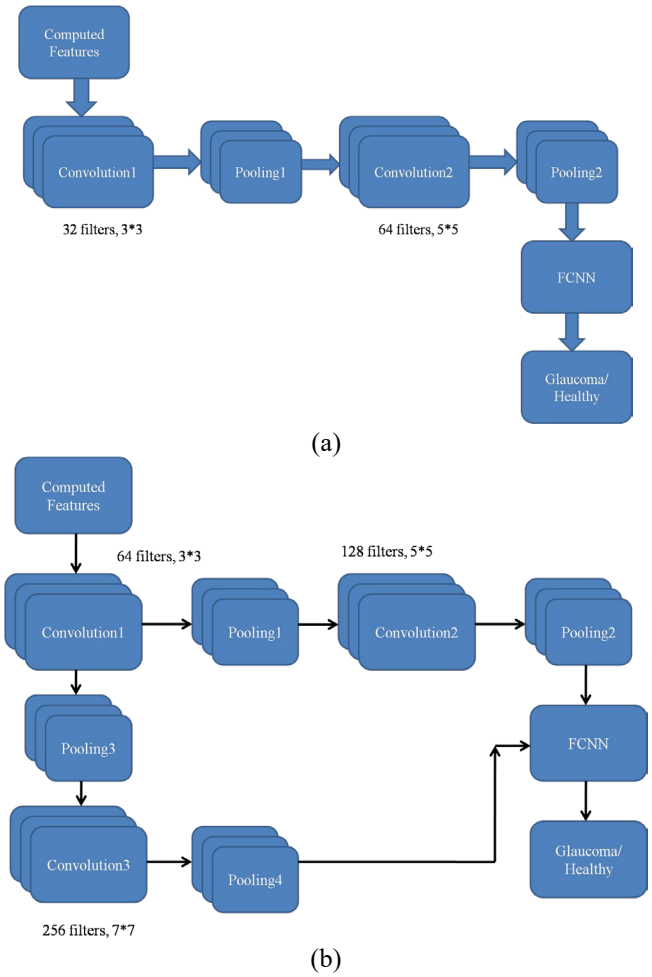

Figure 4 (a). Existing LeNET for feature classifications into either Glaucoma or healthy image (b) Proposed MLNET for feature classifications into either Glaucoma or healthy image

Figure 5 (a) shows the healthy retinal images which are classified by the proposed MLNET classifier and Figure 5 (b) shows the Glaucoma retinal images which are classified by the proposed MLNET classifier.

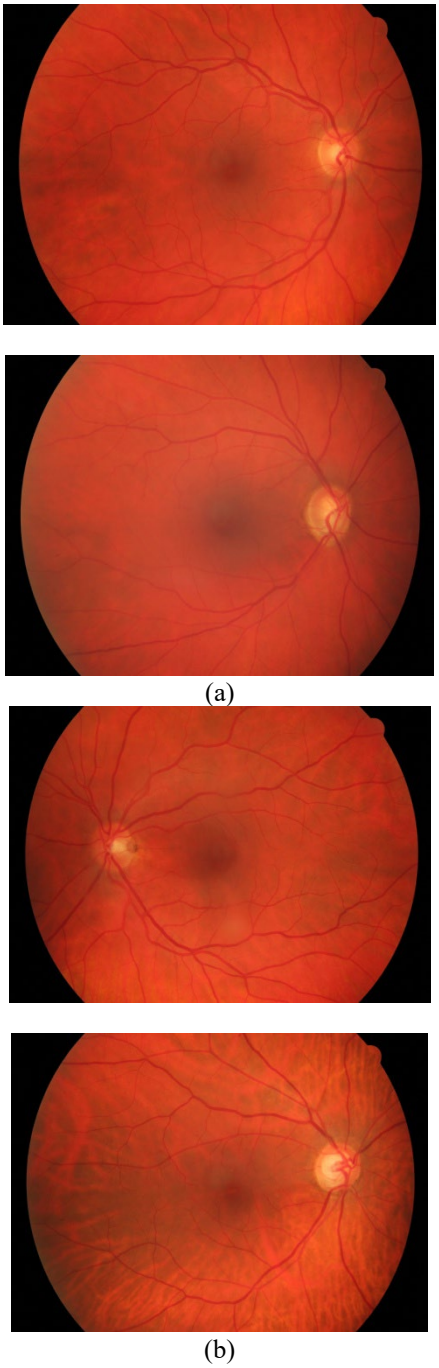

Figure 5. MLNET outputs (a) Healthy retinal images (b) Glaucoma retinal images

4. Results and Discussion

Utilizing MATLAB R2019 version simulating software, the performance of the suggested Glaucoma classification system is assessed. In this paper, the efficacy of

the glaucoma and healthy retinal image categorization system is assessed using the following metrics. The ratio of correctly categorized healthy images to the total number of healthy retinal images is known as the Healthy Image Classification Rate, or HICR. The ratio of the total number of retinal images with glaucoma to the number of correctly categorized images is known as the Glaucoma Image Classification Rate, or GICR.

$$Healthy\ Image\ Classification\ Rate\ (HICR) = \frac{Number\ of\ correctly\ classified\ healthy\ images}{Total\ healthy\ retinal\ images}$$

$$Glaucoma\ Image\ Classification\ Rate\ (GICR) = \frac{Number\ of\ correctly\ classified\ Glaucoma\ images}{Total\ Glaucoma\ retinal\ images}$$

The proposed glaucoma classification algorithm achieves an 86.6% HICR on the HRF database and properly diagnoses 13 healthy retinal images out of 15. Additionally, the suggested method obtains 86.6% GICR on HRF database and properly identifies over 15 glaucoma retinal pictures. The research work's proposed glaucoma classification algorithm obtains 93.3% HICR on the RIGA database and properly classifies 42 healthy retinal pictures out of 45. Furthermore, the suggested approach achieves 90% GICR on the RIGA database and accurately identifies 45 glaucoma retinal images over 50.

The categorization rate analysis for both healthy and glaucoma-affected retinal pictures on the HRF and RIGA databases is displayed in Table 1.

Table 1. Classification rate analysis on both HRF and RIGA datasets

Retinal image cases	HRF database HRF dataset				RIGA database RIGA dataset			
	Total number of retinal images	Correctly classified retinal images	HICR in %	GICR in %	Total number of retinal images	Correctly classified retinal images	HICR in %	GICR in %
Healthy retinal images	15	13	86.6	-	45	42	93.3	-
Glaucoma retinal images	15	13	-	86.6	50	45	-	90
Total images	30	26	-	-	95	89	-	-

Table 2 is the HICR and GICR computational comparisons using the proposed MLNET structure.

Table 2. HICR and GICR computational comparisons

Database	HICR (%)	GICR (%)
HRF	86.6	93.3
RIGA	86.6	**90**

The performance of the proposed Glaucoma classification approach is also evaluated by segmenting the OD region, which is necessary for Glaucoma detection, using the following metrics.

$$Sensitivity(Sey) = \frac{P1}{P1 + N2}$$

$$Specificity\ (Spy) = \frac{N1}{N1 + P2}$$

$$Classification\ Accuracy\ (CA) = \frac{P1 + N1}{P1 + N1 + P2 + N2}$$

Whereas, P1 and P2 are the correctly located OD pixels and non-OD pixels in retinal images, P3 and P4 are the incorrectly located OD pixels and non-OD pixels in retinal images.

All of these metrics are expressed as percentages and are used to evaluate the performance of the proposed MLNET structure for OD area segmentation in retinal pictures.

Table 3 shows the simulation results of retinal images from the HRF dataset for OD segmentation using the traditional LeNet structure. The conventional LeNet structure obtains 94.09% Sey, 93.31% Spy and 94.27% CA for OD region segmentation of the retinal images on HRF dataset.

Table 3. Simulation results of retinal images on HRF dataset for OD segmentation using conventional LeNet structure

Retinal imaging orders in HRF dataset	Simulation values determined in %		
	Sey	Spy	CA
H1	94.29	94.39	94.39
H2	94.19	94.19	94.86
H3	94.20	93.28	93.28

H4	93.87	93.46	93.97
H5	93.67	92.98	95.18
H6	94.29	91.38	95.56
H7	94.98	90.20	94.29
H8	93.67	91.76	94.78
H9	93.58	95.29	93.91
H10	94.20	96.18	92.57
Mean value	**94.09**	**93.31**	**94.27**

Figure 6 is the pictorial representation of simulation results of retinal images on HRF dataset for OD segmentation using conventional LeNet structure.

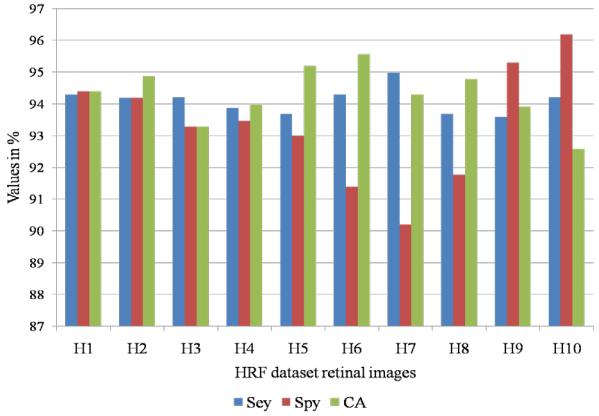

Figure 6. Pictorial representation of simulation results of retinal images on HRF dataset for OD segmentation using conventional LeNet structure

Table 4 is the simulation results of retinal images on RIGA dataset for OD segmentation using conventional LeNet structure. The conventional LeNet structure obtains **94.31**% Sey, **94.34**% Spy and **94.75**% CA for OD region segmentation of the retinal images on RIGA dataset.

Table 4. Simulation results of retinal images on RIGA dataset for OD segmentation using conventional LeNet structure

Retinal imaging orders in HRF dataset	**Simulation values determined in %**		
	Sey	**Spy**	**CA**
R1	93.29	94.29	95.29
R2	94.98	94.37	95.36
R3	94.28	94.29	95.75
R4	94.36	94.54	94.29
R5	94.87	93.76	94.57
R6	95.29	93.18	93.18
R7	95.27	93.98	94.29
R8	94.40	94.28	95.19
R9	93.18	95.47	94.28
R10	93.19	95.29	95.39
Mean value	**94.31**	**94.34**	**94.75**

Figure 7 is the pictorial representation of simulation results of retinal images on RIGA dataset for OD segmentation using conventional LeNet structure.

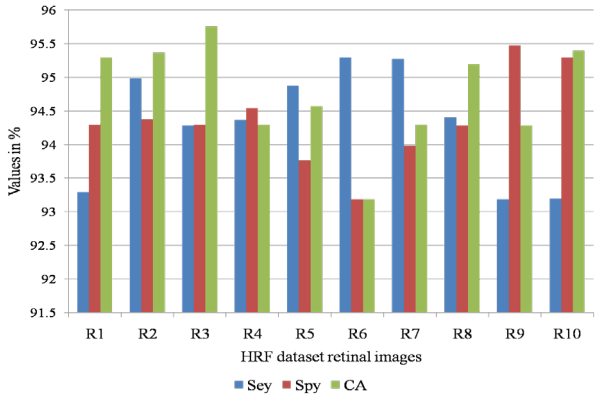

Figure 7. Pictorial representation of simulation results of retinal images on RIGA dataset for OD segmentation using conventional LeNet structure

Table 5 shows the Simulation results of retinal images on HRF dataset for OD segmentation using modified LeNet (MLNET) structure. The proposed MLNET method obtains 100% Sey, 93.7% Spy and 96.6% CA on HRF dataset retinal images.

Table 5. Simulation results of retinal images on HRF dataset for OD segmentation using modified LeNet (MLNET) structure

Retinal imaging orders in HRF dataset	**Simulation values determined in %**		
	Sey	**Spy**	**CA**
H1	95.3	96.3	96.1
H2	95.5	96.1	95.9
H3	96.1	95.8	95.4
H4	95.9	95.4	95.9
H5	96.3	96.7	95.4
H6	96.1	96.4	95.3
H7	95.9	95.9	95.8
H8	95.7	95.3	96.1
H9	96.1	96.8	96.4
H10	96.7	96.1	96.3
Mean value	**95.96**	**96.08**	**95.86**

Figure 8 is the pictorial representations of simulation results of retinal images on HRF dataset for OD segmentation using MLNET structure.

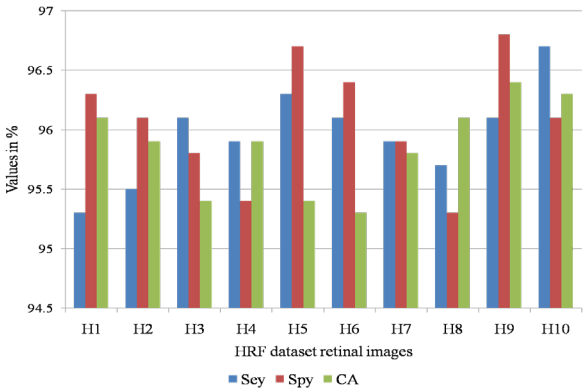

Figure 8. Pictorial representations of simulation results of retinal images on HRF dataset for OD segmentation using MLNET structure

Table 6 shows the Simulation results of retinal images on RIGA dataset for OD segmentation using modified LeNet (MLNET) structure. The proposed RIGA method obtains **95.97**% Sey, **96.03**% Spy and **96.22**% CA on HRF dataset retinal images.

Table 6. Simulation results of retinal images on RIGA dataset for OD segmentation using modified LeNet (MLNET) structure

Retinal imaging orders in HRF dataset	Simulation values determined in %		
	Sey	Spy	CA
R1	96.3	96.3	95.9
R2	96.1	95.9	96.4
R3	95.9	95.3	96.1
R4	95.4	96.1	95.8
R5	96.3	96.9	95.9
R6	96.2	96.3	96.3
R7	95.9	96.1	96.7
R8	96.3	96.8	96.4
R9	95.9	95.4	95.9
R10	95.4	95.2	96.8
Mean value	**95.97**	**96.03**	**96.22**

Figure 9 is the pictorial representations of simulation results of retinal images on HRF dataset for OD segmentation using MLNET structure.

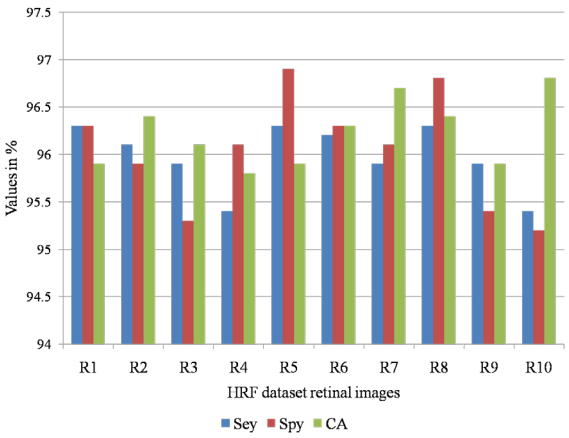

Figure 9. Pictorial representations of simulation results of retinal images on HRF dataset for OD segmentation using MLNET structure

Table 7 shows the performance analysis of the suggested Glaucoma classification system on the HRF and RIGA datasets.

Table 7. Estimation of performance of LeNET and MLNET classifiers

Performance metrics in %	Using conventional LeNet structure		Using proposed MLNET structure	
	HIF dataset	RIGA dataset	HIF dataset	RIGA dataset
Sey	95.96	95.97	94.09	94.31
Spy	96.08	96.03	93.31	94.34
CA	95.86	96.22	94.27	94.75

Table 8 is the OD segmentation performance comparative analysis on HRF dataset.

On the HRF dataset, Naing et al. [17] obtained 93.12% Sey, 93.10% Spy, and 93.17% CA; Radha et al. [18] obtained 93.09% Sey, 93.03% Spy, and 92.46% CA; Shubham Joshi et al. [19] obtained 92.87% Sey, 92.56% Spy, and 92.07% CA; Sudhan et al. [20] obtained 92.36% Sey, 92.19% Spy, and 91.24% CA; Mangipud et al. [21] obtained 92.01% Sey, 91.59% Spy, and 90.85% CA; Guo et al. [22] obtained 91.87% Sey, 90.98% Spy, and 90.57% CA on the HRF dataset; Jiang et al. [23] obtained 91.29% Sey, 89.57% Spy, and 89.27% CA.

Table 8. OD segmentation performance comparative analysis on HRF dataset

Authors	HRF dataset		
	Sey (%)	Spy (%)	CA (%)

Proposed method	**95.96**	**96.08**	**95.86**
Naing et al. (2024)	93.12	93.10	93.17
Radha et al. (2023)	93.09	93.03	92.46
Shubham Joshi et al. (2022)	92.87	92.56	92.07
Sudhan et al. (2022)	92.36	92.19	91.24
Mangipud et al. (2021)	92.01	91.59	90.85
Guo et al. (2020)	91.87	90.98	90.57
Jiang et al. (2019)	91.29	89.57	89.27

Figure 10 is the pictorial representations of OD segmentation performance comparative analysis on HRF dataset.

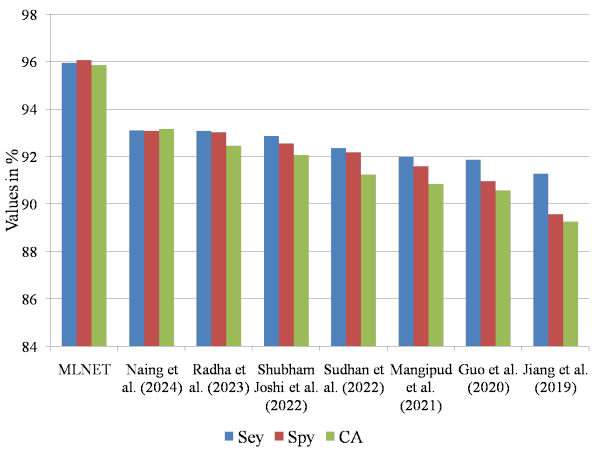

Figure 10. Pictorial representations of OD segmentation performance comparative analysis on HRF dataset

Table 9 is the OD segmentation performance comparative analysis on RIGA dataset.

The traditional techniques On the HRF dataset, Naing et al. [17] obtained 94.29% Sey, 94.07% Spy, and 94.28% CA; Radha et al. [18] obtained 93.19% Sey, 93.16% Spy, and 93.19% CA; Shubham Joshi et al. [19] obtained 92.56% Sey, 92.75% Spy, and 92.56% CA; Sudhan et al. [20] obtained 91.91% Sey, 91.96% Spy, and 91.96% CA; Mangipud et al. [21] obtained 90.34% Sey, 90.43% Spy, and 89.32% CA; Guo et al. [22] obtained 89.29% Sey, 89.95% Spy, and 89.32% CA; and Jiang et al. (2019) obtained 88.38% Sey, 88.18% Spy, and 88.06% CA on HRF dataset.

Table 9. OD segmentation performance comparative analysis on RIGA dataset

Authors	**HRF dataset**		
	Sey (%)	**Spy (%)**	**CA (%)**
Proposed method	**95.97**	**96.03**	**96.22**
Naing et al. (2024)	94.29	94.07	94.28
Radha et al. (2023)	93.19	93.16	93.19
Shubham Joshi et al. (2022)	92.56	92.75	92.56
Sudhan et al. (2022)	91.91	91.96	91.96
Mangipud et al. (2021)	90.34	90.43	90.46
Guo et al. (2020)	89.29	89.95	89.32
Jiang et al. (2019)	88.38	88.18	88.06

Figure 11 is the pictorial representations of OD segmentation performance comparative analysis on RIGA dataset.

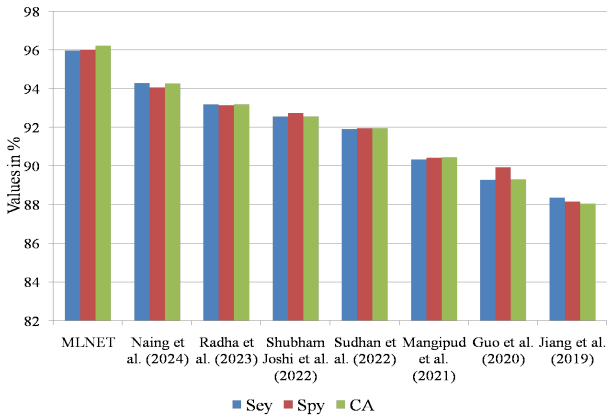

Figure 11. Pictorial representations of OD segmentation performance comparative analysis on RIGA dataset

Table 10 is the classification rates comparisons on HRF dataset with respect to HICR and GICR using the proposed MLNET structure.

Table 10. Classification rates comparisons on HRF dataset

Methods	**HICR (%)**	**GICR (%)**
Proposed MLNET structure	86.6	86.6
Naing et al. (2024)	85.1	85.3
Radha et al. (2023)	84.7	84.1
Shubham Joshi et al. (2022)	83.9	83.2
Sudhan et al. (2022)	82.6	82.0
Mangipud et al. (2021)	81.0	80.9

Figure 12 is the pictorial representations of classification rates comparisons on HRF dataset.

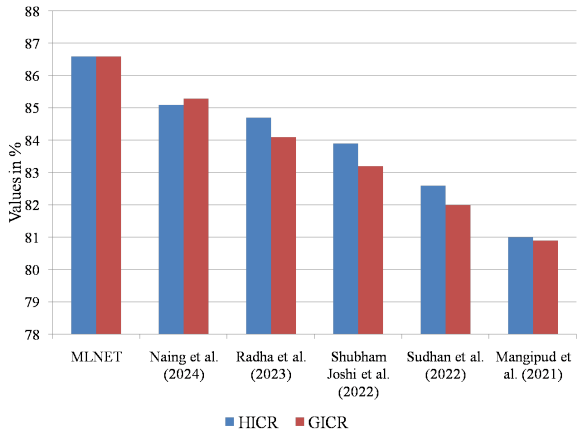

Figure 12. Pictorial representations of classification rates comparisons on HRF dataset

Table 11 is the classification rates comparisons on RIGA dataset with respect to HICR and GICR using the proposed MLNET structure.

Table 11. Classification rates comparisons on RIGA dataset

Methods	HICR (%)	GICR (%)
Proposed MLNET structure	93.3	90
Naing et al. (2024)	91.9	88.9
Radha et al. (2023)	90.7	87.1
Shubham Joshi et al. (2022)	89.7	86.5
Sudhan et al. (2022)	88.4	85.8
Mangipud et al. (2021)	85.9	84.3

Figure 13 is the pictorial representations of classification rates comparisons on RIGA dataset.

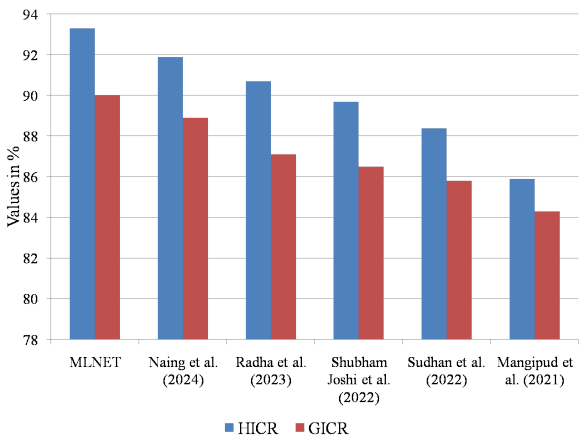

Figure 13. Pictorial representations of classification rates comparisons on RIGA dataset

This research verifies the mean accuracy level of the suggested Glaucoma classification system using the K-fold validation algorithm. Six folds were used in this instance, with one fold serving as the test case and the other five being used to train the system. As a result, the mean accuracy level in this work was produced after a total of six iterations. The K-fold validation for accuracy determination is shown in Figure 14. Iteration 1 has an accuracy rate of 89.9%. Iteration 2 achieves 90.1% accuracy. Iteration 3 has an accuracy rate of 88.9%. Iteration 4 has an accuracy rate of 89.9%. Iteration 5 has an accuracy rate of 89.9%. Iteration 6 has an accuracy rate of 88.7%. The average accuracy is therefore almost 89.5%.

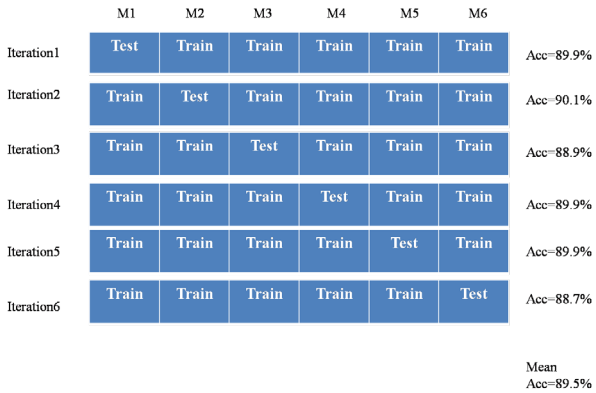

Figure 14. K-fold validation for accuracy determination

5. Conclusion

In this paper, the retinal images are classified into healthy case or Glaucoma case using the conventional LeNET and the proposed MLNET classification architecture. The proposed glaucoma classification algorithm achieves an 86.6% HICR on the HRF database and properly diagnoses 13 healthy retinal images out of 15. Additionally, the suggested method obtains 86.6% GICR on HRF database and properly identifies over 15 glaucoma retinal pictures. The proposed glaucoma classification algorithm obtains 93.3% HICR on the RIGA database and properly classifies 42 healthy retinal pictures out of 45. Furthermore, the suggested approach achieves 90% GICR on the RIGA database and accurately identifies 45 glaucoma retinal images over 50. Retinal pictures from the HRF dataset yield 100% Sey, 93.7% Spy, and 96.6% CA using the suggested MLNET approach. On retinal pictures from the HRF dataset, the suggested RIGA approach achieves 95.97% Sey, 96.03% Spy, and 96.22% CA.

Conflicts of Interest

The authors declare that there is no conflict of interest regarding the publication of this article.

Funding Statement

This research work is not funded by any organization.

Acknowledgements

JR, DK and SE drafted and edited the paper. The tables and graphs in the experimental findings section were contributed by SJ, SS, RU who also conducted the experiments.

References

[1] P.Costa, A. Galdran, A. Smailagic and A. Campilho, "A Weakly-Supervised Framework for Interpretable Diabetic Retinopathy Detection on Retinal Images," IEEE Access, 6, pp. 18747-18758, 2018. 10.1109/ACCESS.2018.2816003

[2] S. Dutta, B. Manideep, S. M. Basha, R. D. Caytiles, N. J. I. J. o. G. Iyengar, and D. Computing, "Classification of diabetic retinopathy images by using deep learning models," Int. Journal of grid and distributed computing, 11(1), pp. 89-106, 2018. 10.14257/ijgdc.2018.11.1.09

[3] S. Kumar and B. Kumar, "Diabetic retinopathy detection by extracting area and number of microaneurysm from colour fundus image," 2018 5th International Conference on Signal Processing and Integrated Networks (SPIN), pp. 359-364, 2018. 10.1109/SPIN.2018.8474264

[4] J. Xu et al., "Automatic Analysis of Microaneurysms Turnover to Diagnose the Progression of Diabetic Retinopathy," IEEE Access, 6, pp. 9632-9642, 2018. 10.1109/ACCESS.2018.2808160

[5] X. Zeng, H. Chen, Y. Luo and W. Ye, "Automated Diabetic Retinopathy Detection Based on Binocular Siamese-Like Convolutional Neural Network," IEEE Access, 7, pp. 30744-30753, 2019. 10.1109/ACCESS.2019.2903171

[6] S. Qummar et al., "A Deep Learning Ensemble Approach for Diabetic Retinopathy Detection," IEEE Access, 7, pp. 150530-150539, 2019. 10.1109/ACCESS.2019.2947484

[7] R. Pires, S. Avila, J. Wainer, E. Valle, M. D. Abramoff, and A. Rocha, "A data-driven approach to referable diabetic retinopathy detection," 96, pp. 93-106, 2019. 10.1016/j.artmed.2019.03.009

[8] B.Antal and A. Hajdu, "An Ensemble-Based System for Microaneurysm Detection and Diabetic Retinopathy Grading," IEEE Transactions on Biomedical Engineering, 59(6), pp. 1720-1726, 2012. 10.1109/TBME.2012.2193126

[9] L. Seoud, T. Hurtut, J. Chelbi, F. Cheriet and J. M. P. Langlois, "Red Lesion Detection Using Dynamic Shape Features for Diabetic Retinopathy Screening," IEEE Transactions on Medical Imaging, 35(4), pp. 1116-1126, 2016. 10.1109/TMI.2015.2509785

[10] Nasrollahi & Rizzo, P 2020, 'Modeling a new dynamic approach to measure intraocular pressure with solitary waves', J. Mech. Behav. Biomed. Mater., vol. 103, pp. 1-9. 10.1016/j.jmbbm.2019.103534

[11] G. Gifta Jerith, P. Nirmal Kumar, "Recognition of Glaucoma by means of Gray Wolf Optimized Neural Network," Multim. Tools Appl. vol. 79 (15-16), pp. 10341-10361, 2020. https://doi.org/10.1007/s11042-019-7224-1

[12] Ferreira, Marcos & Filho, Antonio & Dalília, Alcilene & Silva, Ari & Gattass, Marcelo. "Convolutional neural network and texture descriptor-based automatic detection and diagnosis of Glaucoma," Expert Systems with Applications, vol. 110, 2018. 10.1016/j.eswa.2018.06.010

[13] Bechar, Mohammed & Settouti, Nesma & El Habib Daho, Mostafa & Chikh, Mohammed. "Semi-supervised Super-pixels classification for White Blood Cells segmentation," Conference: 2018 3rd International Conference on Pattern Analysis and Intelligent Systems, pp. 1-8, 2018. 10.1109/PAIS.2018.8598521

[14] Yujie Z, Li Chaoshun, Fu Wenlong, Liu Jie, Yu Tian & Chen Hao. "A modified variational mode decomposition method based on envelope nesting and multi-criteria evaluation," Journal of Sound and Vibration, vol. 468, 115099, 2020. https://doi.org/10.1016/j.jsv.2019.115099

[15] Pavithra P, Manjunath, TC, Lamani, Dharmanna, "Detection of Primary Glaucoma Using ANN with the Help of Back Propagation Algo in Bio-medical Image Processing," Intelligent Communication Technologies and Virtual Mobile Networks, pp.48-63, 2020. 10.1007/978-3-030-28364-3_5

[16] Alghmdi, Hanan & Tang, Hongying & Hansen, Morten & O'Shea, Arrianne & Al turk, Lutfiah & Petö, Tünde, "Measurement of optical cup-to-disc ratio in fundus images for glaucoma screening," IEEE Conference: International Workshop on Computational Intelligence for Multimedia Understanding, vol. 1-5, 2015. 10.1109/IWCIM.2015.7347097.

[17] Naing, SL & Aimmanee, P, "Automated optic disk segmentation for optic disk edema classification using factorized gradient vector flow", Scientific Reports, vol. 14, p. 371, 2024. https://doi.org/10.1038/s41598-023-50908-5

[18] Radha, K, Yepuganti, K & Saritha, S, "Unfolded deep kernel estimation-attention UNet-based retinal image segmentation", Scientific Reports, vol. 13, p. 20712, 2023. https://doi.org/10.1038/s41598-023-48039-y

[19] Shubham Joshi, Partibane Wesam, B, Atef Hatamleh, Hussam Tarazi, Chandra Shekhar Yadav & Daniel Krah 2022, "Glaucoma Detection Using Image Processing and Supervised Learning for Classification", Journal of Healthcare Engineering, vol. 2022, pp. 1-12. https://doi.org/10.1155/2022/2988262

[20] Sudhan, MB, Sinthuja, M, Pravinth Raja, S, Amutharaj, J, Charlyn Pushpa Latha, G, Sheeba Rachel, S, Anitha, T, Rajendran, T & Yosef Asrat Waji, "Segmentation and Classification of Glaucoma Using U-Net with Deep Learning Model", Journal of Healthcare Engineering, vol. 2022, pp. 1-10. 10.1155/2022/1601354

[21] P.S. Mangipudi, H.M. Pandey and A. Choudhary, Improved optic disc and cup segmentation in Glaucomatic images using deep learning architecture, Multimed Tools Appl. 80, pp. 30143–30163, 2021. https://doi.org/10.1007/s11042-020-10430-6

[22] F. Guo,W. Li, J. Tang, B. Zou and Z. Fan, Automated glaucoma screening method based on image segmentation and feature extraction, Medical, & Biological Engineering & Computing, 10, 2020. 10.1007/s11517-020-02237-2

[23] Y. Jiang, N. Tan and T. Peng, Optic disc and cup segmentation based on deep convolutional generative adversarial networks, IEEE Access, 7, pp. 64483–64493, 2019. 10.1109/ACCESS.2019.2917508